Profiling transboundary aerosols over Taiwan and assessing their radiative effects

Sheng-Hsiang Wang,[1,2,3] Neng-Huei Lin,[1,*] Ming-Dah Chou,[1] Si-Chee Tsay,[3] Ellsworth J. Welton,[3] N. Christina Hsu,[3] David M. Giles,[4,3] Gin-Rong Liu,[1] and Brent N. Holben[3]

[1]National Central University, Chung-Li, Taiwan
[2]University of Maryland, College Park, Maryland, USA
[3]Goddard Space Flight Center, NASA, Greenbelt, Maryland, USA
[4]Sigma Space Corporation, Lanham, Maryland, USA

Submitted to the Journal of Geophysical Research – Atmospheres

Special section on East Asian Study of Tropospheric Aerosols and Impact on Regional Climate

*Corresponding author address: Dr. Neng-Huei Lin, Department of Atmospheric Sciences, National Central University, Chung-Li 320, Taiwan

Email:nhlin@cc.ncu.edu.tw

Tel and Fax : +886-3-4254069

Abstract

A synergistic process was developed to study the vertical distributions of aerosol optical properties and their effects on solar heating using data retrieved from ground-based radiation measurements and radiative transfer simulations. Continuous MPLNET and AERONET observations were made at a rural site in northern Taiwan from 2005 to 2007. The aerosol vertical extinction profiles retrieved from ground-based lidar measurements were categorized into near-surface, mixed, and two-layer transport types, representing 76% of all cases. Fine-mode (Ångström exponent, α, ~1.4) and moderate-absorbing aerosols (columnar single-scattering albedo ~0.93, asymmetry factor ~0.73 at 440 nm wavelength) dominated in this region. The column-integrated aerosol optical thickness at 500 nm (τ_{500nm}) ranges from 0.1 to 0.6 for the near-surface transport type, but can be doubled in the presence of upper-layer aerosol transport. We utilize aerosol radiative efficiency (ARE; the impact on solar radiation per unit change of τ_{500nm}) to quantify the radiative effects due to different vertical distributions of aerosols. Our results show that the ARE at the top-of-atmosphere (-23 W m^{-2}) is weakly sensitive to aerosol vertical distributions confined in the lower troposphere. On the other hand, values of the ARE at the surface are -44.3, -40.6 and -39.7 W m^{-2} for near-surface, mixed, and two-layer transport types, respectively. Further analyses show that the impact of aerosols on the vertical profile of solar heating is larger for the near-surface transport type than that of two-layer transport type. The impacts of aerosol on the surface radiation and the solar heating profiles have implications for the stability and convection in the lower troposphere.

INDEX TERMS: 0305 Atmospheric Composition and Structure: Aerosols and particles; 0360 Atmospheric Composition and Structure: Transmission and scattering of radiation; 1637

Global Change: Regional climate change; 3359 Atmospheric Processes: Radiative processes; 0345 Atmospheric Composition and Structure: Pollution: urban and regional (0305 , 0478 , 4251)

KEYWORDS: aerosol vertical distribution, aerosol optical properties, direct aerosol radiative effect

1. Introduction

Aerosols affect the Earth's energy budget by scattering and absorbing radiation (the "direct effect") and by modifying the life cycle and properties of clouds (the "indirect effect"). The complex spatial, temporal, chemical composition, physical size and shape, as well as the optical characteristics of the atmospheric aerosols cause large uncertainties in the estimation of the effects of aerosols on climate [*IPCC*, 2007; *CCSP,* 2009].

Information on the vertical distribution and the optical properties of tropospheric aerosols is required for radiative transfer calculations and is of paramount importance in understanding the effects of aerosols on climate [e.g., *Kaufman et al.,* 1997a; *Haywood and Ramaswamy*, 1998 and references therein]. To date, only a few recent studies have taken into consideration the detailed aerosol vertical distribution that was retrieved using remote-sensing techniques in estimating the radiative effects of aerosols [e.g., *Johnson et al.*, 2008; *McFarlane et al.*, 2009]. However, the often observed multi-layer aerosol transport over East Asia [e.g., *Murayama et al.*, 2004; *Chiang et al.*, 2007] can cause uncertainties in the estimation of aerosol effects on the regional climate.

Several studies have demonstrated the ability to retrieve the vertical profiles of aerosol extinction using a combination of Micro Pulse Lidar (MPL) and Sun/sky radiometer measurements of aerosol optical thickness (τ) [e.g., *Welton et al.,* 2000; *Welton et al.*, 2002; *Campbell et al.,* 2003; *Schmid et al.*, 2006; *Hayasaka et al.*, 2007; *He et al.*, 2008]. The NASA Micro Pulse Lidar Network (MPLNET) [*Welton et al.*, 2001] provides coordinated and standardized observations of aerosol vertical distribution from a federated network of MPL systems collocated with the NASA Aerosol Robotic Network (AERONET) [*Holben et al.*, 1998] Sun/sky radiometers. However, at the present time only a subset of all MPLNET sites have collected more than a few continuous years of data. Thus, long-term studies of MPLNET derived aerosol vertical distribution are only just now becoming possible. In this paper, we first demonstrate a long-term database obtained from an AERONET and MPLNET collocated site to study aerosol vertical distributions of optical properties. The data acquisition rate is used to evaluate the state-of-the-art measurement strategy for this site.

In this study, we present a synergistic process to characterize the vertical distributions of aerosols, their optical properties, and the direct aerosol radiative effect (DARE) using ground-based remote-sensing and a radiative transfer model. Three years (from 2005 to 2007) of vertical aerosol extinction (σ, km^{-1}) profiles and column-integrated aerosol optical properties were derived from lidar and Sun/sky radiometers measurements at a rural location in Taiwan. We categorized the aerosol extinction profiles into three types, representing the major characteristics of the vertical distribution of aerosol over Taiwan. The integration with trajectories analysis, space-based remote-sensing and radiative transfer calculations provided insights into understanding the relationships between the vertical distribution of aerosol, the transport mechanism, its optical properties and its radiation effects.

2. Measurements and Data Usage

2.1. Site Description

The aerosol data used in this study were taken from observations at National Central University (NCU) in Chungli City (24.97°N, 121.18°E; 133 m above sea level), 50 km south of Taipei, Taiwan. Chungli is a medium-sized city with a population of ~360,000. NCU serves as a rural site because it is located at the western edge of Chungli with no significant emission sources nearby. The meteorological conditions are characterized by the southwesterly Asian monsoon in the summer and the northeasterly monsoon in the winter. The weather is humid and cloudy during the summer, but dry and relatively clear during the winter. Studies have shown that northern Taiwan is located on the pathway of the pollution transport from Asia to the Pacific Ocean during pollution outbreaks [*Liu et al.*, 2006; *Chiang et al.*, 2007].

2.2. Sun/sky radiometer

The CIMEL Electronique CE-318 Sun/sky radiometer measurements reported in this paper were made by instruments that participate in AERONET [*Holben et al.*, 1998]. A brief description of the instrumentation and its calibration can be found on the AERONET website (http://aeronet.gsfc.nasa.gov/). The Sun/sky radiometer makes direct solar irradiance measurements with a 1.2° full field of view every 15 min at 340, 380, 440, 500, 675, 870, 940, and 1020 nm (nominal wavelength, λ). The uncertainty of the measured τ, due primarily to the calibration uncertainty, is ± 0.01 for $\lambda > 440$nm and ± 0.02 for $\lambda \leq 440$nm. In addition to the direct solar irradiance measurements, the Sun\sky radiometer measures the sky radiance at four wavelengths (440, 675, 870, and 1020 nm) along the solar almucantar (i.e., at a constant elevation angle, with varied azimuth angles) up to eight times a day. The sky radiance measurements are used to retrieve additional columnar aerosol properties including volume size distribution, phase function, real and imaginary components of the refractive index, effective particle radius, single-scattering albedo (ω), and the asymmetry factor (g), which are routinely computed with the AERONET inversion algorithms [*Dubovik and King*, 2000; *Dubovik et al.*, 2006; *Holben et al.*, 2006]. Specifically, the retrievals of ω and the imaginary part of the refractive index are further limited to $\tau_{440nm} \geq 0.4$ due to an increased uncertainty in the absorption properties of the inversion retrieval during a lower aerosol loading in the atmosphere [*Dubovik et al.* 2002a and 2002b]. The uncertainty in the retrieved ω is estimated to be ±0.03.

Two Sun/sky radiometers are located at the NCU campus. One of them is jointly operated by the Taiwan Environmental Protection Administration (EPA) and the Department of Atmospheric Sciences, NCU (hereafter referred to as the EPA-NCU site). The other radiometer, located within ~200 m of the EPA-NCU site, is operated by the Center for Space and Remote Sensing Research, NCU (hereafter referred to as the NCU_Taiwan site).

2.3. Micro Pulse Lidar (MPL)

The EPA-NCU MPL system is a member of the NASA MPLNET project (http://mplnet.gsfc.nasa.gov/). The MPL [*Spinhirne et al.*, 1995] is a compact and eye-safe single wavelength (527 nm) elastic backscatter lidar system capable of determining the range of both aerosols and clouds by firing a short pulse of laser light and measuring the time-of-flight from the pulse transmission to the reception of the returned signal. Our system supports long-term measurements with 1-minute time resolution and 0.075 km vertical resolution. The standard instrument design and level 1 signal processing are described in detail by *Campbell et al*. [2002] and *Welton et al.* [2002]. Real time data products (level 1.5, no quality assurance) are provided on a next day basis, and include identification of multiple cloud layer heights (base and top), the planetary boundary layer (PBL) height, and the height of the highest aerosol layer. Time resolutions for each product are: clouds (1 minute), aerosols (20 minutes), and PBL (5 minutes). The derivation of level 1.5 aerosol properties is based on the algorithm by *Welton et al*. [2000] where the AERONET level 1.5 aerosol optical thickness is used as the constraint to solve for the lidar ratio and the extinction and optical thickness profiles from the cloud screened 20-minute signal averages. The mean uncertainty in MPLNET retrieved extinction is ±0.015 km^{-1}. However, the assumption of a constant lidar ratio (extinction-backscatter ratio) throughout a profile causes a larger uncertainty in the derivation of extinction when there is multi-layer aerosol transport [*Welton et al.*, 2002].

Level 2 quality-assured data products are currently under development, and beta level 2a aerosol data were made available for this study. Level 2a processing uses AERONET level 2 [*Smirnov et al.,* 2000; *Dubovik et al.*, 2002a; *Holben et al.*, 2006] aerosol optical thickness, and bad data are discarded in order to assure high quality. MPLNET data are discarded if one or several of the following occurs: the data were acquired outside the preferred instrument temperature range (22.5 ± 2 °C, for this instrument); the lidar ratio error was larger than 30%; less than 80% of the signals in the 20-minute average were cloud free; or the signal-to-noise ratio was higher than 20% directly above the top of the aerosol layer. MPLNET aerosol products have been validated in a number of studies, and the most recent and comprehensive one was by *Schmid et al.* [2006], which indicated the accuracy of beta level 2a MPLNET aerosol extinction profiles to within 20%.

2.4. Data Usage

The three years (from 2005 to 2007) of aerosol data (τ, α , ω, g, and σ) used in this study were based on the AERONET level 2 and MPLNET beta level 2a data sets, which were quality-assured and were only for cloud-free conditions. Figure 1a shows the number of days in a month when the AERONET level 1 (not cloud-screened or quality-assured) and level 2 data were available at the two sites (EPA-NCU and NCU_Taiwan). The AERONET data from EPA-NCU were not available prior to 18 July 2006. Therefore, the data from the NCU_Taiwan site were used for this period. Three major issues affected the continuity of this data set: (1) relatively few data were obtained from NCU_Taiwan because this site did not follow closely the AERONET standard measurement procedure for continuous monitoring prior to 2009, (2) the Level 2 data from NCU_Taiwan were eliminated due to an instrumental issue (i.e., moisture contamination) during January and June 2006, and (3) a regular calibration was performed for the EPA-NCU instrument during September and October 2007, and there were no observations during these two months.

In Figure 1b, the MPLNET level 1 data set reveals the continuous measurements (day and night) with a total of 1034 days over 3 years (a data acquisition rate of 94 %). On the other hand, the MPLNET beta level 2a shows only 189 days over 3 years (a data acquisition rate of ~17%), because the MPLNET beta level 2a retrieval relies on AERONET level 2 data, which is cloud-screened and quality-assured data. In addition, if we consider a perfect measurement period (August 2006 to July 2007) when the MPL and the Sun/sky radiometer operated continuously, then the AERONET level 2 and MPLNET level 2a data for the EPA-NCU site are 175 (~48%) and 119 (~33%) days per year, respectively. The value of 33% represents the percentage of days with clear sky in a year and also the maximum available days based on the measurement strategy for this site.

Daily mean profiles were computed when at least three σ profiles were available in a UTC day. There were a total of 145 daily mean σ profiles available at NCU for the analysis of the vertical characteristics of the aerosol. The daily mean values of τ, α , *ω*, and *g* for the 145 days were calculated from

$$\bar{x}_{\lambda} = \frac{1}{n} \cdot \sum_{i=1}^{n} x_{\lambda,i} \qquad (1)$$

where $x_{\lambda,i}$ is the i^{th} instantaneous observation for aerosol optical property x at the wavelength λ, and n is the number of observations in a day. Due to a large variation in the days available in each month, it is not proper to interpret the seasonal variation of the vertical distributions of aerosol; and therefore, a classification for the vertical distribution of aerosol has been applied in this study.

3. Methodology

3.1. Vertical Distribution Classifications of Aerosols

The σ profiles derived from the MPL observations were classified into three types in order to describe the complex characteristics of aerosol vertical distributions. The rules for the classification of these three types are listed in Table 1. Figure 2 shows the σ profiles of the three types and the corresponding temperature and dew-point profiles. In Figures 2a–2c, the daily mean σ profiles conform to the rules shown in Table 1, but the instantaneous σ profiles show perturbations. The corresponding temperature and dew point temperature profiles shown in Figures 2d–2f are the soundings at the Taipei station (~30 km north of NCU). In Figures 2a and 2d (Type 1), the vertical distribution of mean σ is restricted to within 2.0 km above ground level (AGL), which is known as the mixed layer [*Stull*, 1998]. The sounding profiles show a strong and stable inversion layer around 2.0 km, which confines aerosols to the region below 2.0 km. On the other hand, in Figure 2e, the sounding profiles show an inversion layer around 1.7 km, which confines most of the aerosols in the mixing layer (Figure 2b). In addition, a weaker mean σ was observed in the lower free atmosphere (the layer of 1.7 - 2.8 km height in Figure 2e). This suggests that the source of aerosol in the lower free atmosphere could be caused by three mechanisms: (1) the local aerosols lift up to the free atmosphere from the mixing layer, (2) the aerosols remain in the residual layer and (3) the long-range transport of the aerosols in the free atmosphere.

Normally, mechanisms (1) and (2) can be identified based on the time evolution of normalized relative backscatter (NRB) obtained from the MPLNET level 1 data. However, to define the third mechanism, we need assistance from other information (such as back trajectory, sounding and satellite data). For the Type 2 case (Figures 2b and 2e), the weaker inversion layer of around 1.7 km and the well following ambient temperature and dew-point profiles below 2.8 km imply the exchange of air mass between the mixing layer and the lower free atmosphere, as evidenced by the NRB. However, in this case the contribution from the long-range transport of aerosol in the free atmosphere is hard to separate. Compared to the Figure 2b, Figure 2c (Type 3) shows enhanced σ between 2 and 4 km, which is most likely due to the long-range transport aerosol in the lower atmosphere. The strong inversion layer around 1.8 km, and the diverging ambient temperature and dew-point profiles between 2 and 3 km in Figure 2f provide evidence of the different sources of air mass in the vertical distribution. According to the characteristics of the vertical distributions of aerosol, in this paper Type 1 will refer to near-surface aerosol transport, Type 2 will refer to near-surface aerosol transport with upper-layer convective mixing/dispersion of aerosol, and Type 3 will refer to two-layer aerosol transport.

3.2. Radiative Transfer Model Calculations

We investigated the aerosol radiative effect using the radiative transfer model of *Chou and Lee* [1996] and *Chou and Suarez* [1999]. The model includes the absorption by ozone, water vapor, oxygen and CO_2, as well as the absorption and scattering by clouds, aerosols, and molecules (Rayleigh scattering). Fluxes are integrated virtually over solar spectrum, ranging from 0.175 μm to 10 μm, which is divided into 11 bands in the model. Depending upon the nature of the absorption, different approaches are applied to different absorbers. A more detailed description of this model can be found elsewhere [*cf. Chou and Suarez,* 1999; *Chou et al.,* 2006].

Data input to this model includes the vertical profiles of temperature, humidity, ozone, surface albedo and the aerosol optical properties. In this study, we constructed 121 pressure layers in vertical, starting from the ground surface and ending up at the top-of-atmosphere (TOA), in which the layers of 1-81 (from surface to ~6 km AGL with the vertical resolution of 0.075 km) were based on the vertical profile of the MPL measurement. The temperature and humidity profiles taken from the 6-hourly NCEP reanalysis [*Kalnay et al.*, 1996] were interpolated to the model layers. The vertical ozone distribution was based on the climatology values. The daily surface albedo data [*Schaaf et al.*, 2002] were derived from the moderate resolution imaging spectroradiometer (MODIS) Collection 5 combined Level 3 16-day Albedo Products (MCD43B, http://ladsweb.nascom.nasa.gov/).

The seven Cimel channels are located within the 11 bands of the radiative transfer model of *Chou et al.* [2006]. We derived the aerosol optical properties of a model band by averaging the AERONET-retrieved aerosol optical properties (i.e., τ, ω and g) within the band. For those model bands outside the range of the Cimel channels, the aerosol optical properties were set to be equal to those of the nearest Cimel channels [*Chou et al.*, 2006]. Thus, the vertical profiles of τ were derived by scaling the daily mean τ at each Cimel channel with the MPLNET-retrieved σ vertical profiles at 527 nm. For the ω and g, we assumed constant values in the vertical distribution. Because of the presence of clouds, aerosol retrievals may not be complete in a day. It is therefore not feasible to derive the aerosol radiative effect using diurnal variations of the aerosol optical properties. Instead, we used the daily mean values of aerosol optical properties to derive hourly solar radiation, and then averaged to obtain the corresponding daily mean solar radiation.

The direct aerosol radiative effect (DARE, W m^{-2}) is defined as the change in net radiation due to aerosols in clear-sky given by

$$DARE(p) = F_{wa}(p) - F_{na}(p) \tag{2}$$

where $F_{wa}(p)$ and $F_{na}(p)$ represent the net downward fluxes with and without aerosols at pressure level p. Let $\mathrm{DARE}_{\mathrm{TOA}}$ and $\mathrm{DARE}_{\mathrm{SFC}}$ be the DARE at the TOA and the surface, respectively, the DARE in the atmosphere, $\mathrm{DARE}_{\mathrm{ATM}}$, which is the solar heating of the atmosphere due to aerosols, is then given by

$$DARE_{ATM} = DARE_{TOA} - DARE_{SFC} \tag{3}$$

Finally, the impact of aerosols on the atmospheric heating rate of a layer between p and $p+\Delta p$, $\Delta Q(p)$, is proportional to $DARE(p) - DARE(p+\Delta p)$.

4. Results and Discussion

4.1. Vertical Distribution of Aerosols

Three types of σ profiles were classified based on the conditions described in section 3.1. These 3 types were found in 28, 51, and 31 days, respectively, and comprised 76% of the 145 days. The vertical profiles of the mean and standard deviation of the σ of Types 1–3 are shown in Figures 3a–3c, respectively. Below 337.5 m AGL, no readings of the σ are shown due to the near-field observation limits of our particular MPL [*Campbell et al.*, 2002]. Specifically, the average calculation for the daily σ profiles not only smoothes the profiles, but also eliminates some peak values. In addition, the large standard deviation shows that the classification we applied in this study is an approximation. The following sections provide a brief discussion of the σ profiles type classifications in relation to the backward trajectories for each type.

Type1: Near-surface aerosol transport

In Figure 3a, the mean σ decreases with the increase in height, and is restricted within 2.0 km. The highest σ shows ~0.2 km^{-1} near 0.5 km and decreases to ~0.01 km^{-1} at ~2.0 km. The height of 2 km represents the maximum mixing layer height for Type 1, in which the mixing layer height varies between 1.0 km and 2.0 km as illustrated by the standard deviations of profile. In addition, the fall and winter seasons (September - January) are prevailing seasons for the Type 1 classifications (Figure 3d), but few days were observed in the summer time.

Trajectory analysis has been used to diagnose the movement of pollutants in previous studies [e.g., *Draxler,* 1996; *Wang et al.,* 2007 and references therein]. The Hybrid Single-Particle Lagrangian Integrated Trajectory (HYSPLIT) model, developed by NOAA Air Resources Laboratory [*Draxler and Rolph*, 2003], is applied to calculate air mass back trajectories. The meteorological data used to initialize HYSPLIT is obtained from the NCEP Global Data Assimilation System (GDAS) data set [*Kalnay et al*., 1996]. Figure 4 shows the 5-day backward trajectories of Types 1–3 ending at 0.5 km and 2.5 km above the mean sea level (MSL) over NCU. The altitudes of 0.5 km and 2.5 km present the near-surface and upper-layer air mass transport, respectively. The color table uses in the image denotes trajectory altitudes for the 5-day computational period. The symbols mark the days behind the ending day.

In Type 1 (Figure 4a), the major pathway of the air mass shows the potential aerosol source regions from northeast Asia with trajectories passing over the West Pacific. The four trajectories that strayed from the major pathway correspond to the days in spring and summer as shown in Figure 3d. Most of the trajectories traversed over coastal regions which have been identified as major anthropogenic regions in East Asia [*Street et al.,* 2003]. When the air mass traversed over the ocean during the last two days, the trajectories were found to be mainly within the marine boundary layer (below 1.0 km in the color table). The near surface shallow transport with anthropogenic aerosol (e.g., sulfate and nitrate) over the ocean is expected to have more aerosol water uptake or more aerosol hydroscopic growth [*Seinfeld,* 1986]. In the final half day before ending at NCU, the trajectories pass over northern Taiwan where the local pollutants also contribute to the aerosol loading. In general, the Type 1 classifications are represented by the northerly flow causing a transport belt for air mass advection over long distances towards Taiwan. The σ below 2 km are due to the presence of an abundance of anthropogenic aerosols caused by long-range transport and local pollutants.

Type 2: Near-surface aerosol transport with upper-layer convective mixing/dispersion of aerosols

In Figure 3b, the mean σ decreases with the increase in height, and is restricted to within 4.0 km. The two σ peaks below 1.0 km with a value of ~0.27 km^{-1} illustrated the various maximum σ heights in Type 2 cases. Compared to Type 1, the mean σ profile of Type 2 shows an aerosol layer that is extended up to 4 km. The upper-layer aerosol transport related to the convective mixing/dispersion of aerosols in the free atmosphere is described in Section 3.1. Figure 3e shows the diverse coverage for months in Type 2, in which the most frequent occurred month is July.

The 5-day backward trajectories at 0.5 km of NCU for Type 2 are shown in Figure 4b. Most of the trajectories come from the north of Taiwan via a route similar as that of Type 1. This implies that similar atmospheric features may represent the near-surface aerosol transport observed in both Types 1 and 2. In addition, some of the southern and eastern trajectories related to the summer season also belong to Type 2. These trajectories originate from the clean marine atmosphere and from the atmosphere in Southeast Asia where low pollution emissions are found during the summer. As a result, local emissions might be the essential source of the near-surface aerosol layer. For the upper-layer transport, as shown in Figure 4d, the trajectories ending at 2.5 km show various routes and are mostly westerly in winter and southeasterly in summer. These westerly trajectories will have traveled over densely populated and industrialized areas. In these regions the air motion transports the aerosols to the free atmosphere by means of frontal lifting [e.g., *Bey et al.*, 2001; *Liang et al.*, 2004]. On the other hand, the southeasterly trajectories which originated above the West Pacific Ocean, pass over the Philippines, the South China Sea, off the coast of southern China, and then over southern Taiwan. Most likely the marine pathway has less long-range transport aerosols from the continental regions, but a higher possibility of local aerosol aloft due to the enhanced vertical convection mixing of aerosols in summer. However, the aerosol particles that lift towards the free atmosphere are not able to be seen in the HYSPLIT simulation because of the coarse resolution of the meteorological data, as well as the terrain data.

Type 3: Two-layer aerosol transport

The two-layer transport structure of aerosols has been reported in the literature [e.g., *Welton et al.*, 2002; *Murayama et al.*, 2004; *He et al.,* 2008; *Johnson et al.,* 2008; *McFarlane et al.,* 2009]. An MPL retrieved mean σ profile with a 2-layer structure (Type 3) over NCU is shown in Figure 3c. In contrast to Type 2, Type 3 shows significant upper-layer (2–4 km) aerosol transport. The prominent σ of ~0.09 km^{-1} at 2.4 km reveals almost one-half the amount of ~0.21 km^{-1} near the ground, thereby emphasizing the importance of upper-layer transport. We suggest that the 2-layer aerosol transport is not only due to considerable quantities of long-range transport aerosols exist in the free atmosphere but also the fact that inversion layer plays a significant role in preventing the mixing of vertical convective aerosol. Figure 3f shows that except for the unusual occurrence of a frequency of 10 days in October which related to a single event during 11 - 23 October 2006, the most frequent occurrence for 2-layer aerosol transport season take place in spring (March – May), which agrees with previous studies in this region [*Murayama et al.*, 2004; *Chiang et al.*, 2007].

The trajectory distribution of Figure 4c shows a distribution similar to that of Figure 4b, which implies that the near-surface aerosol transport has similar aerosol characteristics for Type 2 and Type 3. In terms of backward trajectories at 2.5 km in Type 3 (Figure 4e), the westerly trajectories suggest that westerlies prevail in the middle troposphere over mid-latitude East Asia. Most of the trajectories originate in Indochina and travel slowly over Southeast China during the last three days. In their pathway, air masses are likely to carry biomass-burning aerosols from Indochina and mix them with the abundance of anthropogenic aerosols from Southeast China and then advect them downwind towards northern Taiwan in the lower free atmosphere. The spatial distribution of τ from the MODIS measurement will be further applied to understand the sources region of aerosol in the next subsection.

4.2. Spatial Distribution of Aerosol Optical Thickness

The MODIS-Aqua Level 3 data with 1°×1° resolution were obtained from the Giovanni online data system (http://disc.sci.gsfc.nasa.gov/giovanni/) in order to analyze the spatial distribution of aerosols in relation to each classified type. MODIS sensors perform near global daily observations of aerosols and eight of the 36 channels (between 0.412 and 2.13 μm) are used to retrieve aerosol properties over land [*Kaufman et al.*, 1997b; *Hsu et al.*, 2004 and 2006; *Levy et al.*, 2007] and ocean [*Tanré et al.*, 1997]. Figure 5 shows that the MODIS-Aqua Level 3 aerosol retrievals of averaged τ at 550 nm for Types 1–3 in the Asian region. Based on the trajectory analysis in previous section, a lead-time of three days was selected for MODIS-retrieved τ to compute the average for each Type of aerosol transport.

The main locations of the large τ in Figures 5a–5c (coastal regions of China, central China, and the Indo-Gangetic Plain) correspond with the relatively densely populated and industrial areas. The potential aerosol sources at NCU for each type can be further illustrated by combining them with the back trajectory in Figure 4. In Figure 5a, the high τ (~1) over the northeastern coast of China (near 35°N, 118°E) have a high probability of contributing to the near-surface aerosol transport in Type 1. On the other hand, it is evident from the Figures 5b and 5c that τ are higher than those over the Asian continent and with a stronger continental outflow over the Yellow Sea (near 36°N, 123°E). According to the suggestion of trajectory analysis, the air masses of the near-surface aerosol transport of Type 2 traversing over the high τ region in northeastern China appear more frequently indicating a higher mean σ of near-surface aerosol transport in Type 2 (Figure 3b). On the other hand, the high τ over southeastern China conform to the potential pollution source regions of the upper-layer aerosol transport in Type 3. The high τ over southeastern China are related to the local emission sources [*Street et al*., 2003] and the transported smoke aerosols from the biomass burning in Southeast Asia in the spring [*Hsu et al*., 2003; *Wang et al.,* 2007].

4.3. Aerosol Optical Thickness and Ångström Exponent

Table 2 shows the average and standard deviations of aerosol optical properties for Types 1–3. The mean values of τ_{500nm} are 0.28, 0.45, and 0.44 for Types 1–3, respectively, and are related to the integrated σ profiles. On the other hand, the $\alpha_{440\text{-}870nm}$ remains nearly constant with a mean of ~1.4 for these 3 types, implying that fine mode particles dominate the pollutants. Fine mode particles are commonly observed in the long-range transport of anthropogenic aerosols [*Eck et al.*, 2005].

Figure 6 presents the scatter plots of the AERONET-retrieved daily mean $\alpha_{440\text{-}870nm}$ vs. τ_{500nm} for Types 1–3. The error bars present a one standard deviation. Basically, most data have $\alpha_{440\text{-}870nm}$ values within the range of 1.0–1.8, except for 2 days with lower $\alpha_{440\text{-}870nm}$ (< 1.0) of Type 2, implying that the common feature of fine mode aerosols dominate the pollutants for those 3 classified types. However, the two days with low $\alpha_{440\text{-}870nm}$ reflect the occurrence of coarse mode particles in Type 2. In the case of lowest $\alpha_{440\text{-}870nm}$ (~0.8) on 5 July 2007 in Figure 6b, the aerosols may possibly have been contaminated by cirrus clouds [*Smirnov et al*., 2000]. The other low $\alpha_{440\text{-}870nm}$ case in Figure 6b happened on 28 January 2007, when an Asian dust storm was reported by Taiwan EPA. In terms of aerosol loading, the ranges of τ_{500nm} show 0.13–0.63, 0.15–1.05, and 0.13–1.17 for Types 1–3, respectively.

Similar minimum values of τ_{500nm} suggest that those 3 classified aerosol profiles can be observed even in a low aerosol loading atmosphere. On the other hand, the cases with τ_{500nm} higher than 0.6 are only found in Types 2 and 3. Those high τ_{500nm} cases are not only caused by the upper-layer aerosol transport but also by the stronger aerosol emission sources shown in Figure 5. Consequently, we suggest that a fairly near-surface aerosol transport can contribute to the daily mean τ_{500nm} reaching as high as 0.6. However, when a daily mean τ_{500nm} greater than 0.6 is observed, it implies that an upper-layer aerosol transport could occur, and that the aerosol vertical distribution should be further considered for estimating the radiative effect of aerosol.

4.4. Single-scattering Albedo and Asymmetry Factor

The estimated DARE of the Earth-atmosphere system has to rely on data sources for ω and g, and especially the data on ω are particularly critical for determining the partition of the DARE between the atmosphere and the underlying surface [*Chou et al.*, 2006]. By definition, ω is obtained by dividing the aerosol scattering coefficient by the aerosol extinction coefficient, and g is the fraction of the incident radiation scattered forward after striking an aerosol. $g = 1$ if 100% of the incident radiation is scattered forward, whereas the $g = 0$ indicates that one half of the incident radiation is forward-scattered while the other half is backscattered. The spectral ω and g for Types 1–3 are plotted in Figure 7. Valid data have been selected by the AERONET level 2 inversion data described in section 2.2, and the numbers of the daily mean for Types 1–3 are 4, 24, and 10 days for ω, and 20, 38, and 19 days for g. Group-mean spectral ω and g are derived by averaging arithmetically all the available daily-mean values of ω and g of a given type. The group-mean and one standard deviation of ω and g at 440 nm for Types 1–3 are listed in Table 2.

In Figures 7a–7c, most of the daily mean ω ranging from 0.90 to 0.98 in any wavelength shows that the aerosols are moderately absorbing. In comparison, *Eck et al.* [2005] indicated that in Beijing (China) and Anmyon Island (Korea) the ranges of ω were within 0.84–0.92 and 0.88–0.95, respectively, suggesting that the aerosols had a stronger scattering property at NCU. The stronger scattering property (higher ω) could be caused by hygroscopic growth but also with other possible aging mechanisms such as gas-to-particle conversion, condensation, and coagulation [*Eck et al.,* 2005].

The characteristic of the ω changing with the increase in wavelength relates to the aerosol types for each individual day as shown in Figures 7a–7c. The relationships between spectral dependence of ω and the key aerosol types (e.g., urban-industrial, biomass-burning, desert dust and marine aerosols) have been described in *Dubovik et al.* [2002a], and are based on eight years of worldwide distributed data from the AERONET network. In Type 1, the characteristics of spectral dependence of ω exhibit two different types of aerosol (Figure 7a). Two days (30 – 31 January 2007) with the ω increasing with the increase in wavelength represented the characteristic of desert dust aerosols [*Dubovik et al.,* 2002a; *Eck et al.,* 2005], and has also been identified as a dust event by the Taiwan EPA announcement. On the other hand, the other two days with the ω decreasing with the increase in wavelength show that the characteristic of the urban-industrial aerosol [*Dubovik et al.,* 2002a], and the values of ω show comparable ranges to those of Anmyon Island in Korea [*Eck et al.,* 2005]. For Type 2, most days presented the urban-industrial aerosol type, but a few days presented the desert dust aerosol type. A case with an extreme low ω, with the characteristic of the ω decreasing with the increase in wavelength was observed on 29 March 2007, which was linked to the biomass-burning aerosols type described in *Dubovik et al.* [2002a]. Compared to Types 1 and 2, Type 3 (Figure 7c) shows lower spectral dependence of ω with higher ω values ranging from ~0.92 to 0.97. This implies that the aerosols in the upper-layer likely have a stronger scattering property. Overall, the spectral dependence of ω shows that the downwind area of Asian continental pollutants is dominated by urban-industrial aerosols of three types. However, the observed desert dust, the biomass-burning and the mixing aerosols emphasize the complex aerosol types in this region.

In Figures 7d–7f, most of the daily mean g ranged from 0.60 to 0.75 in any wavelength inhibit the aerosols tend to scatter more energy forward. The spectral dependence of g decreases with the increase in wavelength, illustrating that the aerosols have more forward scattering in short wavelengths. As to the group-mean spectral g, the slope of g with wavelength in Type 1 is lower than in Types 2 and 3. The lower slope of the spectral g with a higher g_{1020} in Type 1 represents the characteristic of urban-industrial, desert dust and marine aerosols [*Dubovik et al.,* 2002a]. On the other hand, a case (1 April 2007) of Type 3 shows a pronounced decrease of the g to the relatively low values (from $g_{440} = 0.71$ to $g_{1020} = 0.52$) which corresponds to the features of biomass-burning aerosols [*Dubovik et al.,* 2002a].

4.5. Aerosol Radiative Effect and Heating Rate

The scatter plots of the daily mean $\mathrm{DARE_{TOA}}$ and $\mathrm{DARE_{SFC}}$ vs. τ at 500 nm are shown in Figure 8. Straight lines indicate the linear regressions. Each point represents one day.

Circles represent radiative calculations on those days with daily-mean spectral τ, ω and g. Crosses represent calculations on those days where there are only daily-mean spectral τ, but no daily-mean spectral ω and g. Group-mean spectral ω and g are applied in the calculations. Squares represent calculations on those days where there are daily-mean spectral τ and g, but no daily-mean spectral ω. The group-mean spectral ω are applied in the calculations. The DARE is highly linearly correlated with τ_{500nm} with a negative correlation coefficient of > 0.93 for all types of aerosol vertical distributions, indicating that DARE can be reliably estimated from column-integrated τ_{500nm}. However, some points show a significant deviation from the linear regression which is related to the broad ranges of observed ω and g, especially the $DARE_{SFC}$ in Type 3. The large negative deviation of the $DARE_{SFC}$ from the linear regression on 1 April 2007 (Figure 8f) is due to the small ω and g (Figures 7c and 7f). On the other hand, the case of 14 October 2006 with large ω and g shows a weak negative $DARE_{SFC}$. The deviation of DARE from the linear regression can reach up to ±10 W m^{-2}.

At the TOA, the mean values of $DARE_{TOA}$ are -7.1, -11.6, and -11.2 W m^{-2} for Types 1, 2, and 3, respectively. The negative $DARE_{TOA}$ implies that the effect of the reflection of solar radiation due to aerosols is larger than the effect of absorption, and that the net effect is a cooling of the earth-atmosphere system. At the surface, the mean values of $DARE_{SFC}$ are -13.2, -20.3, and -18.7 W m^{-2} for Types 1, 2, and 3. The significant decrease of the solar radiation at the surface is enhanced by the absorption of solar radiation in the atmosphere due to aerosols. The absorption of solar radiation due to aerosols in the atmosphere, $DARE_{ATM}$, is 6.1, 8.7, and 7.5 W m^{-2} for Types 1–3, respectively.

The aerosol radiative efficiency (ARE) is defined as the change of DARE per unit change of τ at 500 nm. This parameter is useful for quantifying and comparing aerosol radiative effects at different places under a wide range of aerosol conditions [*Wang et al.*, 2007 and references therein]. We estimated ARE_{TOA} and ARE_{SFC} from the slopes of the linear regressions shown in Figure 8, in which uncertainties can be explained by root-mean-square (rms). The AREs for Types 1–3 are listed in Table 3. Values of ARE_{TOA} for these three types are very close (~-23 W m^{-2}), indicating that the solar energy budget of the earth-atmosphere system is not overly sensitive to the vertical distributions of aerosols over northern Taiwan. Compared to ARE_{TOA}, the ARE_{SFC} and ARE_{ATM} show relative sensitivity to the vertical distributions of aerosols, with the highest efficiency in Type 1 and the lowest efficiency in Type 3.

A sensitivity study was performed to investigate how the aerosol vertical distributions shaping the computations of ARE under the assumption of unified aerosol optical properties (i.e., fixed column-integrated τ, column-mean ω, and g of moderate-absorbing aerosol) for various profiles. As expected, the results show that all ARE_{TOA}, ARE_{SFC} and ARE_{ATM} increase (i.e., larger negative values for the first two but larger positive value for the last ARE) when more aerosols are elevated to higher levels in various profiles within thin-τ regime. These increases are due to more downwelling solar irradiance available for aerosols to interact at higher levels, leading to enhanced reflection at TOA and absorption in ATM (in turn, dimmed transmission at SFC). However, as the degrees of freedom in aerosol properties increase (e.g., ω, g, τ, in addition to vertical distribution) in model simulations, the variation of AREs becomes complex due to their competing nature for solar irradiance. Since most of aerosols in Types 1–3 are confined in the lower atmosphere (i.e., below 3 km) with moderate absorption, the values of ARE_{TOA} shown in Table 3 are weakly sensitive to aerosol vertical distributions. When the variations of other aerosol properties (*cf.* Figures 3 and 7) come into play (e.g., ω_λ dominant in Type–1 *vs*. Type–2, against their similar vertical distributions; or larger variability of ω_λ and vertical distribution in Type–3 *vs*. Type–2), ARE_{SFC} coupled with ARE_{ATM} reveal relatively larger variability, compared to ARE_{TOA}.

Although we have demonstrated that the vertical distribution of aerosols does not make a significant difference in the estimation of ARE_{TOA}, it does provide information as to the impact of aerosols on the vertical profile of the atmospheric heating rate. Figure 9 shows the vertical distribution of the mean and one standard deviation of ΔQ (K day^{-1}) for Types 1–3. The ΔQ profiles are similar to the σ profiles in Figure 3, with maximum values of 0.37, 0.41, and 0.26 K day^{-1} at around 700 m in height for Types 1–3, respectively. A larger σ implies a higher aerosol concentration, and hence a stronger impact on ΔQ. The ΔQ of Type 3 is smaller than those of Types 1 and 2 below 2 km, indicating that the upper-layer absorbing aerosol transport enhances the upper-layer ΔQ at the expense of reducing the near-surface ΔQ. The nearly constant ΔQ in the vertical implies a weaker impact on the stability and convection. On the other hand, Types 1 and 2 have a larger ΔQ near the surface and, hence, have a larger impact on convection than Type 3.

4.6. Improving ARE Estimates for Two-layer Aerosol Transport

The assumption of a constant column-mean ω and g throughout a two-layer aerosol transport profile may cause an error in the radiative transfer calculations. The coexistence of near-surface and upper-layer aerosol transport as shown from different source regions, implies different ω and g in the vertical distribution. For example, the different ω in the near-surface and upper layers has been observed using airborne measurements over Niamey [*Osborne et al.,* 2008]. Except for aircraft measurement, the currently available retrieval schemes based on ground measurements are unable to resolve vertical variations of ω and g. Nevertheless, the AERONET measurements at a high mountain site at Lulin (23.51°N, 120.92°E; 2862 m MSL; ~180 km south of NCU), can provide useful information on the optical properties of aerosols for the upper layers of Type 3 at NCU under the assumptions of similar backward trajectories and aerosol sources [*Wai et al*., 2008, Figure 3].

The averaged ω and g of Lulin obtained from AERONET were used as surrogate to improve the ARE estimates for the 2-layer aerosol transport. Due to the quality control limitations of the AERONET inversion algorithm, only a few days of level 2 data [*Holben et al.*, 2006] are available for 2007–2008. They occurred in March–May except for one day in August. The available level 2 data give a 4-day averaged $\omega_{440\text{nm}}$ of 0.96 and a 16-day averaged $g_{440\text{nm}}$ of 0.7. Aerosols in the upper layer observed at Lilun exhibited a relatively stronger scattering property and backward scattering, compared to Types 1–3. Here, we apply aerosol optical properties derived from the Sun/sky radiometer at Lulin, to the upper-layer aerosol transport in Type 3 and repeat the simulations of aerosol effect. In this case, the process basically follows the vertical structure of Type 3, but the ω and g for the near-surface aerosol layer were replaced with group-average values of Type 1 and 2 and for upper-layer were replaced with averaged values of Lulin. As a result, the change in the vertical distribution of the ω and g affects on the ARE calculations are shown in Table 3. Compared to the results of Type 3 in Table 3, the redistributions of ω and g in the vertical profiles enhance the negative ARE_{SFC} (surface cooling, ~-3 W m^{-2}) and the positive ARE_{ATM} (atmosphere heating, ~3 W m^{-2}), but have only a minor influence on ARE_{TOA}. In addition, the vertical distribution of ΔQ shows an enhanced ΔQ by up to 0.2 K day^{-1} in the surface layer when near-surface aerosol replaced with the group-mean aerosol ω and g of Types 1 and 2 (shown in Figure 9c). These preliminary results encourage us to approach the 2-layer aerosol transport problems in the future with case studies using the data from EPA-NCU and the Lulin sites.

5. Conclusions

In this study, we presented a synergistic process to determine the vertical distributions of aerosol optical properties and the impact of aerosols on solar heating using ground-based remote-sensing (Micro-pulse lidar and Sun/sky radiometers) and a radiative transfer model. The MPL and Sun/sky radiometer data were taken from observations at a rural site in northern Taiwan and covered a period of three years (2005–2007).

To simplify the complex characteristics of the aerosol vertical distribution, lidar-retrieved aerosol extinction profiles were classified into three types with common characteristics of near-surface aerosol transport. These three types of aerosol profiles account for 76% of the total data base. In general, the common near-surface aerosol transport (0 to 2 km) is related to the northerly air mass with possible long-range transport of aerosols during wintertime. The upper-layer aerosol transport (2 to 4 km) is caused by the convective mixing/dispersion of aerosol in the free atmosphere.

The columnar aerosol optical properties show that the aerosols in this region are dominated by fine mode (Ångström exponent = ~1.40) and moderately absorbing aerosols (ω = ~0.93 and g = ~0.73 at 440 nm), which are typical of urban-industrial aerosols [*Dubovik et al.,* 2002a]. However, frequent perturbations due to desert dust, biomass-burning or mixed aerosols suggest a diversity of aerosol types over the downwind area of the Asian continent. Compared to the ω in the upwind areas (China and Korea), the higher ω in northern Taiwan suggests that anthropogenic aerosols transported near the ocean surface are likely to experience hydroscopic growth. The column-integrated aerosol optical thickness at 500 nm (τ_{500nm}) ranges from 0.1 to 0.6 for near-surface aerosol transport, but can be doubled in the presence of upper-layer aerosol transport.

Absorbing aerosols have the effect of warming the atmosphere and cooling the surface. The sensitivity of solar radiation to a unit change of τ_{500nm}, referred to aerosol radiative efficiency (ARE), was computed at the top of the atmosphere (ARE_{TOA}) and at the surface (ARE_{SFC}). The ARE_{TOA} is not sensitive to the vertical distributions of aerosols, and is approximately -23 W m^{-2} for the three types of aerosol profiles. On the other hand, the ARS_{SFC} is relatively sensitive to the vertical distribution of aerosols, and is -44.3, -40.6 and -39.7 W m^{-2} for the near-surface, mixed and two-layer transport types, respectively. The difference is caused primarily by the difference in ω; surface transport type aerosols have the smallest ω, and the two-layer transport type aerosols have the largest ω. Correspondingly, the impact of aerosols on the vertical profile of solar heating is the largest for the near-surface transport type and the smallest for the two-layer transport type. Since any changes of solar heating in the atmosphere and at the surface affect the stability of the atmosphere, different aerosol transport type will have different impact on the atmospheric stability, convection, and regional climate.

The coexistence of near-surface and upper-layer aerosol transports infers different aerosol characteristics in the vertical distribution. This study introduce a method, using Sun/sky radiometer observation at the high-altitude station, Lulin (2862 m), to further assist in estimating the upper-layer aerosol optical properties (ω and g) and improve the ARE calculations for the two-layer transport type of aerosols. Using the proposed method, the recalculated $\mathrm{ARE}_{\mathrm{SFC}}$ and $\mathrm{ARE}_{\mathrm{ATM}}$ are enhanced by 3 W m^{-2}, and the solar heating is enhanced by up to 0.2 K day^{-1} in the surface layers. This analysis shows the sensitivity of the vertical distribution of aerosol optical properties for estimating the aerosol radiative effect.

Acknowledgments

This work was supported by the National Science Council of Taiwan under contracts No. 97-2752-M-008-011-PAE, 96-2752-M-008-007-PAE, 97-2745-M-008-010, and 96-2745-M-008-005, and by the Taiwan Environmental Protection Administration under contracts No EPA-97-U1L1-02-101 and EPA-98-FA11-03-A015. The NASA MPLNET and AERONET are funded by the NASA Earth Observing System and Radiation Sciences Program. The authors gratefully acknowledge the NOAA Air Resources Laboratory for the provision of the HYSPLIT transport and dispersion model used in this publication. Special thanks to the scientists (NASA/GSFC) and technicians (NCU) responsible for consulting, operating and maintaining the instrumentation that generated this high-quality data set and ultimately enabled this paper to be written; these colleagues include Tom Eck, Timothy Berkoff, James Campbell, Larry Belcher, Ferret Kuo, and Eric Chia.

References

Bey, I., D. J. Jacob, Jennifer. A. Logan, and R. M. Yantosca (2001), Asian chemical outflow to the Pacific in spring: Origins, pathways, and budgets, *J. Geophys. Res.*, 106(D19), 23,097–23,113.

Campbell, J. R., D. L. Hlavka, E. J. Welton, C. J. Flynn, D. D. Turner, J. D. Spinhirne, V. S. Scott, and I. H. Hwang (2002), Full-Time, Eye-Safe Cloud and Aerosol Lidar Observation at Atmospheric Radiation Measurement Program Sites: Instruments and Data Processing, *J. Atmos. Oceanic Technol.*, 19, 431-442.

Campbell, J. R., E. J. Welton, J. D. Spinhirne, Q. Ji, S.-C. Tsay, S. J. Piketh, M. Barenbrug, and B. N. Holben (2003), Micropulse lidar observations of tropospheric aerosols over northeastern South Africa during the ARREX and SAFARI 2000 dry season experiments, *J. Geophys. Res.*, 108(D13), 8497, doi:10.1029/2002JD002563.

CCSP (2009), *Atmospheric Aerosol Properties and Climate Impacts,* A Report by the U.S. Climate Change Science Program and the Subcommittee on Global Change Research. [Mian Chin, Ralph A. Kahn, and Stephen E. Schwartz (eds.)]. National Aeronautics and Space Administration, Washington, D.C., USA, 128 pp.

Chiang, C.-W., W.-N. Chen, W.-A. Liang, S. K. Das, J.-B. Nee (2007), Optical properties of tropospheric aerosols based on measurements of lidar, sun-photometer, and visibility at Chung-Li (25˚N, 121˚E), *Atmos. Environ.*, 41, 4128-4137.

Chou, M.-D., and K. T. Lee (1996), Parameterizations for the absorption of solar radiation by water vapor and ozone, *J. Atmos. Sci.*, 53, 1203–1208.

Chou, M. D., and M. J. Suarez (1999), A solar radiation parameterization for atmospheric studies, *NASA Tech. Memo., NASA-TM-1999-10460,* vol. 15, 40pp.

Chou, M.-D., P.-H. Lin, P.-L. Ma, and H.-J. Lin (2006), Effects of aerosols on the surface solar radiation in a tropical urban area, *J. Geophys. Res.*, 111, D15207, doi:10.1029/2005JD006910.

Draxler, R. R. (1996), Boundary layer isentropic and kinematic trajectories during the August 1993 North Atlantic Regional Experiment Intensive, *J. Geophys. Res.*, 101(D22), 29,255–29,268.

Draxler, R. R., and G. Rolph (2003), HYSPLIT4 (HYbrid Single-Particle Lagrangian Integrated Trajectory) model, Air Resour. Lab., Natl. Oceanic and Atmos. Admin., Silver Spring, Md. (Available at http://www.arl.noaa.gov/ready/hysplit4.html).

Dubovik, O., and M. D. King (2000), A flexible inversion algorithm for retrieval of aerosol optical properties from Sun and sky radiance measurements, *J. Geophys. Res.*, 105(D16), 20,673–20,696.

Dubovik, O., B. N. Holben, T. F. Eck, A. Smirnov, Y. J. Kaufman, M. D. King, D. Tanre, and I. Slutsker (2002a), Variability of absorption and optical properties of key aerosol types observed in worldwide locations, *J. Atmos. Sci.,* 59, 590-608.

Dubovik, O., B. N. Holben, T. Lapyonok, A. Sinyuk, M. I. Mishchenko, P. Yang, and I. Slutsker (2002b), Non-spherical aerosol retrieval method employing light scattering by spheriods, *Geophys. Res. Lett.,* 29, 54-1 - 54-4.

Dubovik, O., et al. (2006), Application of spheroid models to account for aerosol particle nonsphericity in remote sensing of desert dust, *J. Geophys. Res.*, 111, D11208, doi:10.1029/2005JD006619.

Eck, T. F., et al. (2005), Columnar aerosol optical properties at AERONET sites in central eastern Asia and aerosol transport to the tropical mid-Pacific, *J. Geophys. Res.*, 110, D06202, doi:10.1029/2004JD005274.

Hayasaka, T., S. Satake, A. Shimizu, N. Sugimoto, I. Matsui, K. Aoki, and Y. Muraji (2007), Vertical distribution and optical properties of aerosols observed over Japan during the Atmospheric Brown Clouds–East Asia Regional Experiment 2005, *J. Geophys. Res.*, 112, D22S35, doi:10.1029/2006JD008086.

Haywood, J. M., and V. Ramaswamy (1998), Global sensitivity studies of the direct radiative forcing due to anthropogenic sulfate and black carbon aerosols, *J. Geophys. Res.*, 103(D6), 6043– 6058.

He, Q., C. Li, J. Mao, A. K.-H. Lau, and D. A. Chu (2008), Analysis of aerosol vertical distribution and variability in Hong Kong, *J. Geophys. Res.*, 113, D14211, doi:10.1029/2008JD009778.

Holben, B. N., T. F. Eck, I. Slutsker, D. Tanre, J. P. Buis, A. Setzer, E. Vermote, J. A. Reagan, Y. J. Kaufman, T. Nakajima, F. Lavenu, I. Jankowiak and A. Smirnov (1998), AERONET: a federated instrument network and data archive for aerosol characterization, *Rem. Sens. Environ.*, *66*, 1-16.

Holben, B. N., T. F. Eck, I. Slutsker, A. Smirnov, A. Sinyuk, J. Schafer, D. Giles and O. Dubovik (2006), Aeronet's Version 2.0 quality assurance criteria, *Proc. SPIE*, 6408, 64080Q, doi:10.1117/12.706524.

Hsu, N. C., J. R. Herman, and S.-C. Tsay (2003), Radiative impacts from biomass burning in the presence of clouds during boreal spring in southeast Asia, *Geophys. Res. Lett.*, 30(5), 1224, doi:10.1029/2002GL016485.

Hsu, N. C., S.-C. Tsay, M. D. King and J. R. Herman (2004), Aerosol properties over bright-reflecting source regions, *IEEE Trans. Geosci. Rem. Sens.*, 42, 557-569.

Hsu, N. C., S.-C. Tsay, M. D. King and J. R. Herman (2006), Deep Blue retrievals of Asian aerosol properties during ACE-Asia, *IEEE Trans. Geosci. Rem. Sens.*, 44, 3180-3195.

Intergovernmental Panel on Climate Chang (IPCC) (2007), Climate Change 2007, Working Group I Report "The Physical Science Basis", edited by S. Solomon et al., *Cambridge Univ. Press*, New York.

Johnson, B. T., B. Heese, S. A. McFarlane, P. Chazette, A. Jones, and N. Bellouin (2008), Vertical distribution and radiative effects of mineral dust and biomass burning aerosol over West Africa during DABEX, *J. Geophys. Res.*, 113, D00C12, doi:10.1029/2008JD009848.

Kalnay, E., et al. (1996), The NCEP/NCAR 40-year reanalysis project, *Bull. Amer. Meteor. Soc.,* 77, 437-470.

Kaufman, Y. J., D. Tanre, H. R. Gordon, T. Nakajima, J. Lenoble, R. Frouin, H. Grassl, B. M. Hermann, M. D. King, and P. M. Teillet (1997a), Passive remote sensing of tropospheric aerosol and atmospheric correction for the aerosol effect, *J. Geophys. Res.*, 102, 16,815–16, 830, doi:10.1029/97JD01496.

Kaufman, Y. J., D. Tanré, L. A. Remer, E. Vermote, A. Chu and B. N. Holben (1997b), Remote sensing of tropospheric aerosol from EOS-MODIS over the land using dark targets and dynamic aerosol models, *J. Geophys. Res.*, 102, 17051-17067.

Levy, R. C., L. A. Remer, S. Mattoo, E. F. Vermote and Y. J. Kaufman (2007), Second-generation operational algorithm: Retrieval of aerosol properties over land from inversion of Moderate Resolution Imaging Spectroradiometer spectral reflectance, *J. Geophys. Res.*, 112, D13211, doi:10.1029/2006JD007811.

Liang, Q., L. Jaegle´, D. A. Jaffe, P. Weiss-Penzias, A. Heckman, and J. A. Snow (2004), Long-range transport of Asian pollution to the northeast Pacific: Seasonal variations and transport pathways of carbon monoxide, *J. Geophys. Res.*, *109,* D23S07, doi:10.1029/2003JD004402.

Liu, C.-M., C.-Y. Young, and Y.-C. Lee (2006), Influence of Asian dust storms on air quality in Taiwan, *Sci. of the Total Environ.*, 368, 884-897.

McFarlane, S. A., E. I. Kassianov, J. Barnard, C. Flynn, and T. P. Ackerman (2009), Surface shortwave aerosol radiative forcing during the Atmospheric Radiation Measurement Mobile Facility deployment in Niamey, Niger, *J. Geophys. Res.*, 114, D00E06, doi:10.1029/2008JD010491.

Murayama, T., D. Müller, K. Wada, A. Shimizu, M. Sekiguchi, and T. Tsukamoto (2004), Characterization of Asian dust and Siberian smoke with multi-wavelength Raman lidar over Tokyo, Japan in spring 2003, *Geophys. Res. Lett.*, 31, L23103, doi:10.1029/2004GL021105.

Osborne, S. R., B. T. Johnson, J. M. Haywood, A. J. Baran, M. A. J. Harrison, and C. L. McConnell (2008), Physical and optical properties of mineral dust aerosol during the Dust and Biomass-burning Experiment, *J. Geophys. Res.*, 113, D00C03, doi:10.1029/2007JD009551.

Schaaf, C. B., et al. (2002), First Operational BRDF, Albedo and Nadir Reflectance Products from MODIS*, Remote Sens. Environ.*, 83, 135-148.

Schmid, B., R. Ferrare, C. Flynn, R. Elleman, D. Covert, A. Strawa, E. Welton, D. Turner, H. Jonsson, J. Redemann, J. Eilers, K. Ricci, A. G. Hallar, M. Clayton, J. Michalsky, A. Smirnov, B. Holben, and J. Barnard (2006), How well do state-of-the-art techniques measuring the vertical profile of tropospheric aerosol extinction compare?, *J. Geophys. Res.*, 111, D05S07, doi:10.1029/2005JD005837.

Seinfeld J. H. (1986), *Atmospheric chemistry and physics of air pollution*, 738 pp., Wiley, New York, USA.

Smirnov A., B. N. Holben, T. F. Eck, O. Dubovik, and I. Slutsker (2000), Cloud screening and quality control algorithms for the AERONET database, *Remote Sens. Environ.*, 73, 337-349.

Spinhirne, J. D., J. A. R. Rall, and V. S. Scott (1995), Compact eye safe lidar systems, *Rev. Laser Eng.,* 23, 112-118.

Streets, D. G., et al. (2003), An inventory of gaseous and primary aerosol emissions in Asia in the year 2000, *J. Geophys. Res.*, 108(D21), 8809, doi:10.1029/2002JD003093.

Stull, R. B. (1988), *An introduction to boundary layer meteorology*, Kluwer Academic Pulishers, Dordrecht, 2-3.

Tanré, D., Y. J. Kaufman, M. Herman and S. Mattoo (1997), Remote sensing of aerosol over oceans from EOS-MODIS**,** *J. Geophys. Res.,* 102, 16971-16988.

Wai, K. M., N.-H. Lin, S.-H. Wang, and Y. Dokiya (2008), Rainwater chemistry at a high-altitude station, Mt. Lulin, Taiwan: Comparison with a background station, Mt. Fuji, *J. Geophys. Res.*, 113, D06305, doi:10.1029/2006JD008248.

Wang, S.-H., N.-H. Lin, M.-D. Chou, and J.-H. Woo (2007), Estimate of radiative forcing of Asian biomass-burning aerosols during the period of TRACE-P, *J. Geophys. Res.*, 112, D10222, doi:10.1029/2006JD007564.

Welton, E. J., et al. (2000), Ground-based lidar measurements of aerosols during ACE-2: Instrument description, results, and comparisons with other ground-based and airborne measurement, *Tellus 52B*, 636-651.

Welton, E. J., J. R. Campbell, J. D. Spinhirne, and V. S. Scott (2001), Global monitoring of clouds and aerosols using a network of micro-pulse lidar systems, in Lidar Remote Sensing for Industry and Environmental Monitoring, U. N. Singh, T. Itabe, N. Sugimoto, (eds.), *Proc. SPIE*, 4153, 151-158.

Welton, E. J., K. J. Voss, P. K. Quinn, P. J. Flatau, K. Markowicz, J. R. Campbell, J. D. Spinhirne, H. R. Gordon, and J. E. Johnson (2002), Measurements of aerosol vertical profiles and optical properties during INDOEX 1999 using micropulse lidars, *J. Geophys. Res.*, 107(D19), 8019, doi:10.1029/2000JD000038.

Figure captions

Figure 1. Histogram of the number of days in the month for: (a) AERONET and (b) MPLNET data sets. The light gray and dark gray color bars present level 1 and level 2 data, respectively, for both of the AERONET and the MPLNET data sets. The black color bar presents the MPLNET level 2 dataset with data from Types 1–3 only.

Figure 2. Examples of aerosol extinction (km^{-1}) profiles obtained by MPL at EPA-NCU for: (a) Type 1 (12-Nov-2006), (b) Type 2 (13-Feb-2007) and (c) Type 3 (15-Oct-2006). The blue line is the daily-averaged profile and the red lines present all profiles on that day. Below 375.0 m, no readings are shown due to the near-field observation limits of MPL. Examples of the ambient (Square point) and dew point (dot point) temperature (°C) profiles obtained by Taipei sounding station (~ 30 km north of NCU) at 00UTC for: (d) Type 1 (12-Nov-2006), (e) Type 2 (13-Feb-2007) and (f) Type 3 (15-Oct-2006). The dashed lines between two points present continuously sampling in the vertical distribution, otherwise invalid values are noted.

Figure 3. Profiles of the mean aerosol extinction with one standard deviation derived from the MPLNET observations at EPA-NCU for (a) Type 1, (b) Type 2 and (c) Type 3, with corresponding monthly total number of days for (d) Type 1, (e) Type 2 and (f) Type 3.

Figure 4. Five-day backward trajectories of NCU for (a) Type 1 starting at 500 m, (b) Type 2 starting at 500 m, (c) Type 3 starting at 500 m, (d) Type 2 starting at 2500 m, and (e) Type 3 starting at 2500 m. Each trajectory starts at 00 UTC. Trajectory altitudes (based on the mean sea level, in meters) are denoted by the color scale.

Figure 5. Composite MODIS-Aqua aerosol Deep-Blue and Dark-Target retrievals of $\tau_{550\mathrm{nm}}$

averaged for (a) Type 1, (b) Type 2, and (c) Type 3. The third day before the case days based on the potential pollution source regions has been applied in these plots.

Figure 6. Scatterplots of τ_{500nm} vs. $\alpha_{440\text{–}870nm}$ at NCU for (a) Type 1, (b) Type 2 and (c) Type 3. The error bars indicate the one standard deviation.

Figure 7. The AERONET inversion data (ω and g) at 440, 675, 870, 1020 nm at NCU for (a) ω of Type 1, (b) ω of Type 2, (c) ω of Type 3, (d) g of Type 1, (e) g of Type 2, and (f) g of Type 3. The daily-mean spectral ω and g are shown as cross points and thin lines. The group-mean spectral ω and g are shown as black circles and bold lines.

Figure 8. Scatterplots of DARE at TOA vs. τ at 500 nm for (a) Type 1, (b) Type 2, and (c) Type 3. Scatterplots of DARE at the surface vs. τ_{500nm} for (d) Type 1, (e) Type 2, and (f) Type 3. Circles represent radiative calculations based on daily-mean spectral ω and g, crosses represent data based on only group-mean spectral ω and g, and squares represent data based on daily-mean spectral g and group-mean spectral ω.

Figure 9. The vertical distribution of the mean and one standard deviation of the impact of aerosols on the atmospheric heating rate ΔQ (K day^{-1}) over NCU for (a) Type 1, (b) Type 2 and (c) Type 3 (red lines). The green line* and the blue line** show the improved ΔQ profiles for Type 3. See Table 3 for detailed descriptions of * and **.

Table 1. The classification rules for daily mean aerosol extinction (σ) profiles

Type 1	1. The column-integrated τ_{527nm} greater than 0.1 2. No σ are detected above 6 km AGL* 3. A remarkable and isolated near surface aerosol layer
Type 2	1. Same as rules 1–3 in Type 1 2. Above the near surface aerosol layer, presenting a weaker aerosol layer with vertical aerosol mixing
Type 3	1. Same as rules 1–3 in Type 1 2. Above the near surface aerosol layer, presenting another remarkable and isolated aerosol layer 3. The joint between the two layers shows low σ

*According to long-term MPL observations of EPA-NCU, most atmospheric aerosols exist below 6 km AGL at this site.

Table 2. The aerosol optical thickness (τ) at 500 nm, Ångström exponent (α) at 440 - 870 nm, single-scattering albedo (ω) at 440 nm, and asymmetry factor (g) at 440 nm retrieved from Sun/sky radiometer measurements

Type	Days	τ_{500nm}		$\alpha_{440-870nm}$		ω_{440nm}		g_{440nm}	
		mean	std	mean	std	mean	std	mean	std
Type 1	28	0.28	0.14	1.40	0.17	0.92	0.02	0.72	0.02
Type 2	51	0.45	0.22	1.40	0.18	0.95	0.02	0.73	0.02
Type 3	31	0.44	0.26	1.43	0.15	0.95	0.02	0.73	0.02

Table 3. Aerosol Radiative Efficiency (ARE) of TOA, ATM and SFC for Types 1–3.

	ARE_{TOA}	ARE_{ATM}	ARE_{SFC}
Type 1	-23.3	+21.0	-44.3
Type 2	-22.6	+18.0	-40.6
Type 3	-22.9	+16.8	-39.7
Type 3 (Lulin1*)	-23.1	+19.8	-42.9
Type 3 (Lulin2**)	-24.2	+16.9	-41.1

Unit: W m^{-2}

[*] Values of ω and g at the upper-layer and the near-surface layer of Type 3 were replaced with the mean values from the Lulin site and Type 1, respectively.

[**] Values of ω and g at the upper-layer and the near-surface layer of Type 3 were replaced with the mean values from the Lulin site and Type 2, respectively.

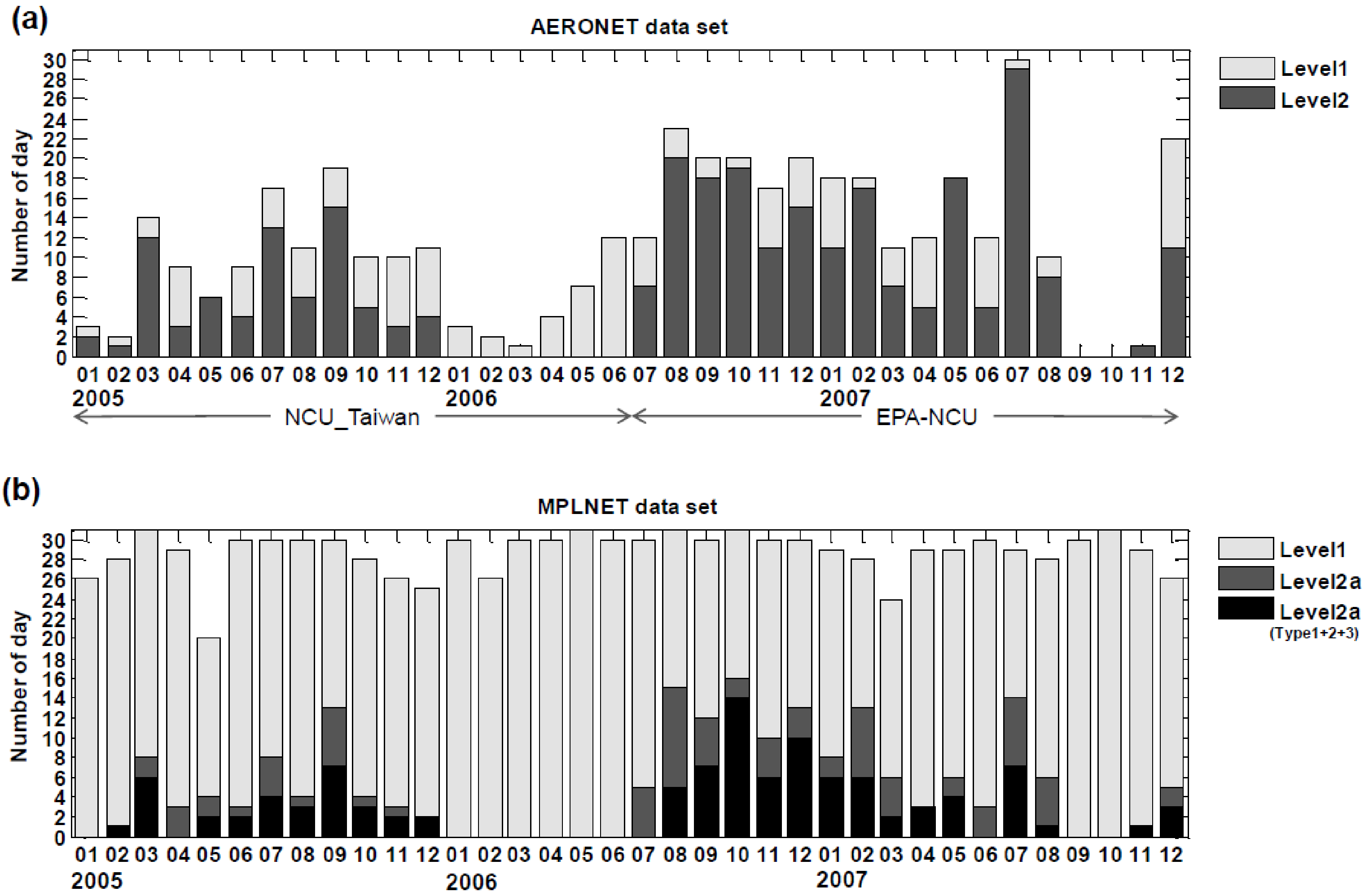

Figure 1. Histogram of the number of days in the month for: (a) AERONET and (b) MPLNET data sets. The light gray and dark gray color bars present level 1 and level 2 data, respectively, for both of the AERONET and the MPLNET data sets. The black color bar presents the MPLNET level 2 dataset with data from Types 1–3 only.

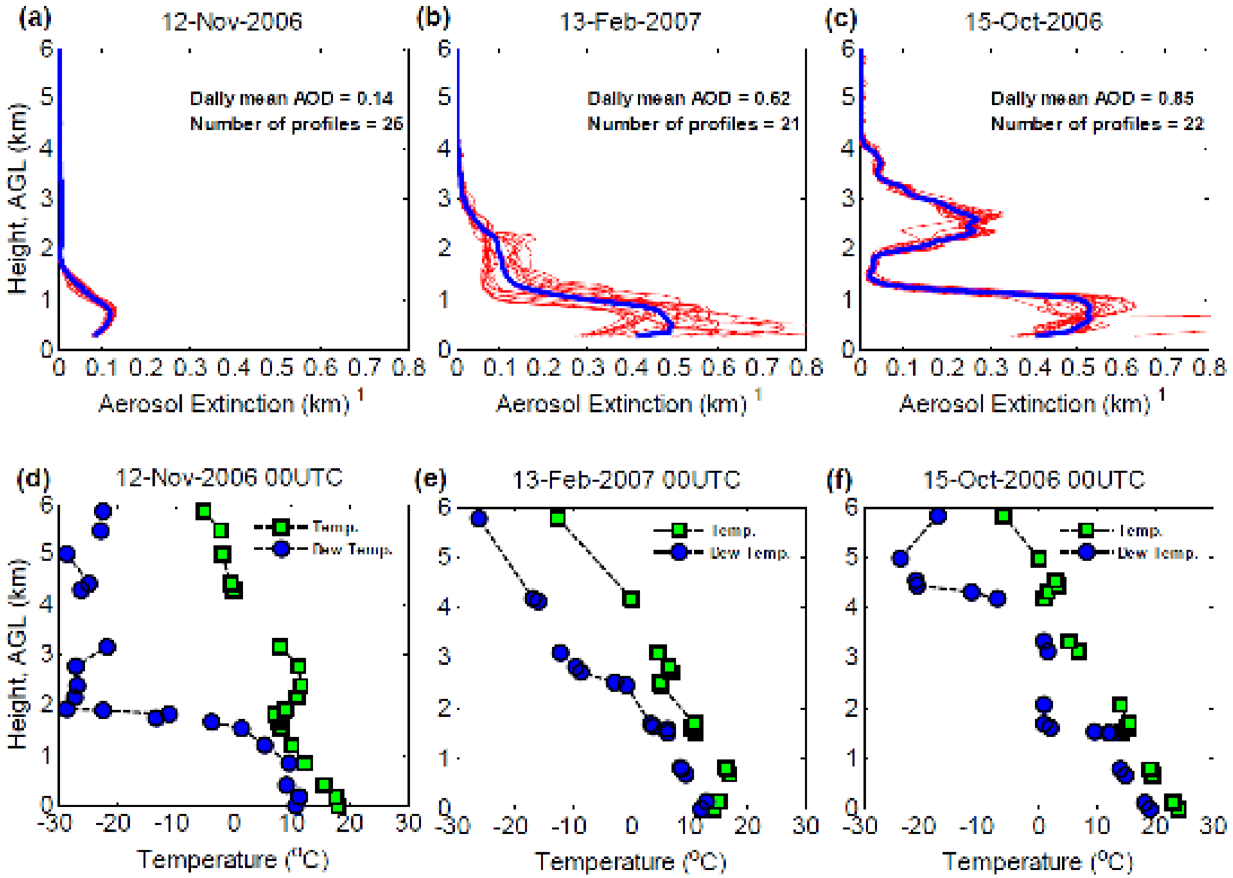

Figure 2. Examples of aerosol extinction (km^{-1}) profiles obtained by MPL at EPA-NCU for: (a) Type 1 (12-Nov-2006), (b) Type 2 (13-Feb-2007) and (c) Type 3 (15-Oct-2006). The blue line is the daily-averaged profile and the red lines present all profiles on that day. Below 375.0 m, no readings are shown due to the near-field observation limits of MPL. Examples of the ambient (Square point) and dew point (dot point) temperature (°C) profiles obtained by Taipei sounding station (~ 30 km north of NCU) at 00UTC for: (d) Type 1 (12-Nov-2006), (e) Type 2 (13-Feb-2007) and (f) Type 3 (15-Oct-2006). The dashed lines between two points present continuously sampling in the vertical distribution, otherwise invalid values are noted.

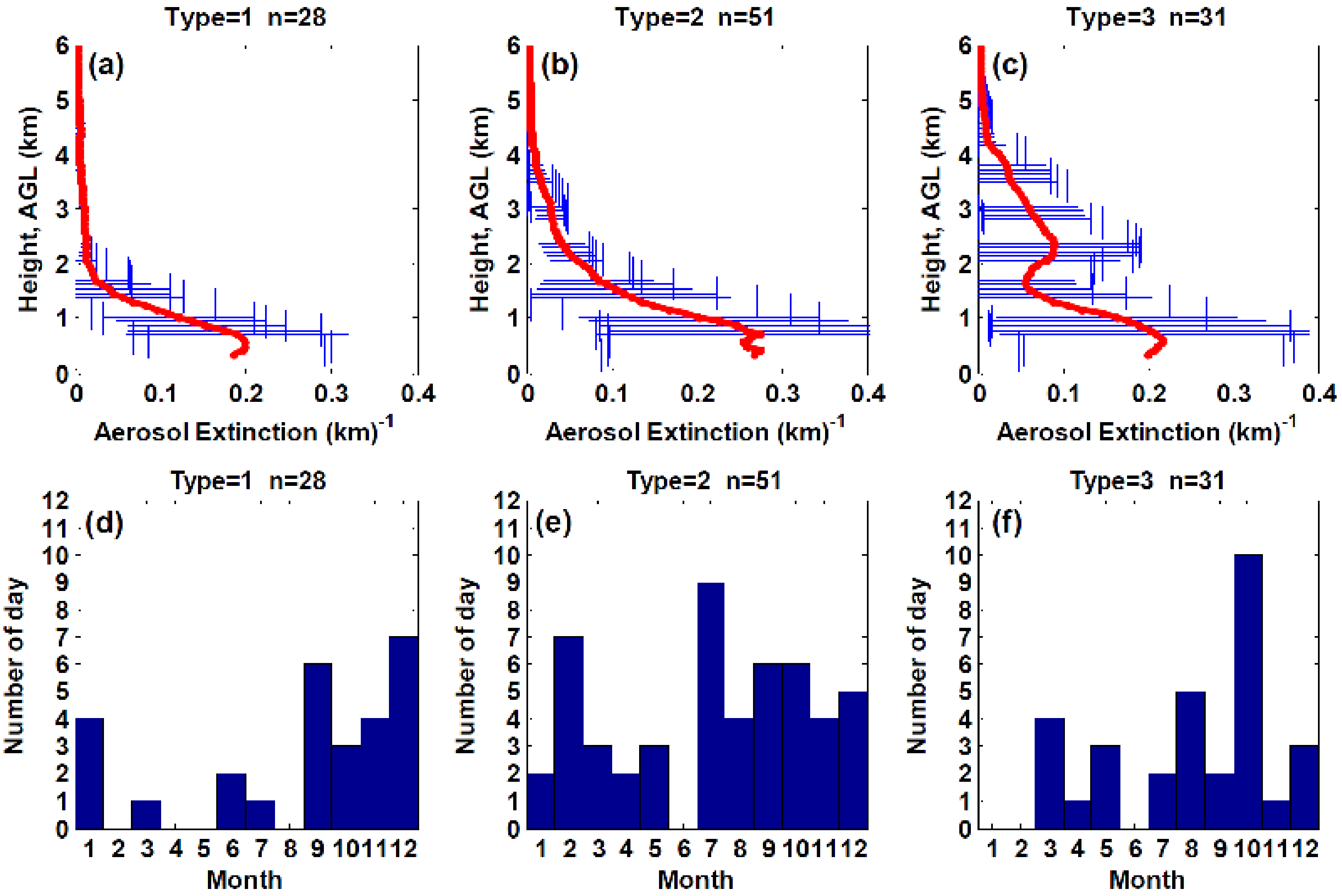

Figure 3. Profiles of the mean aerosol extinction with one standard deviation derived from the MPLNET observations at EPA-NCU for (a) Type 1, (b) Type 2 and (c) Type 3, with corresponding monthly total number of days for (d) Type 1, (e) Type 2 and (f) Type 3.

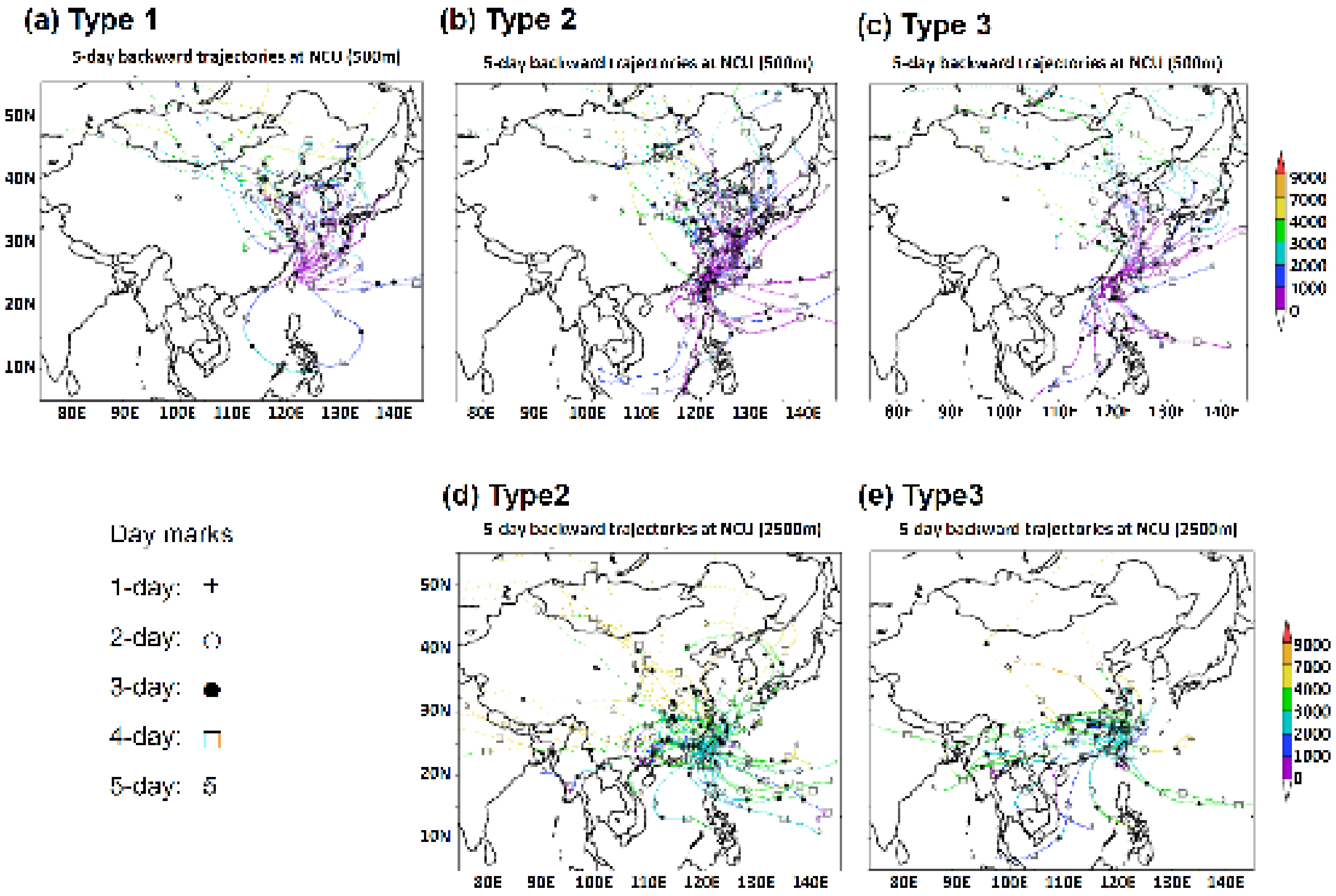

Figure 4. Five-day backward trajectories of NCU for (a) Type 1 starting at 500 m, (b) Type 2 starting at 500 m, (c) Type 3 starting at 500 m, (d) Type 2 starting at 2500 m, and (e) Type 3 starting at 2500 m. Each trajectory starts at 00 UTC. Trajectory altitudes (based on the mean sea level, in meters) are denoted by the color scale.

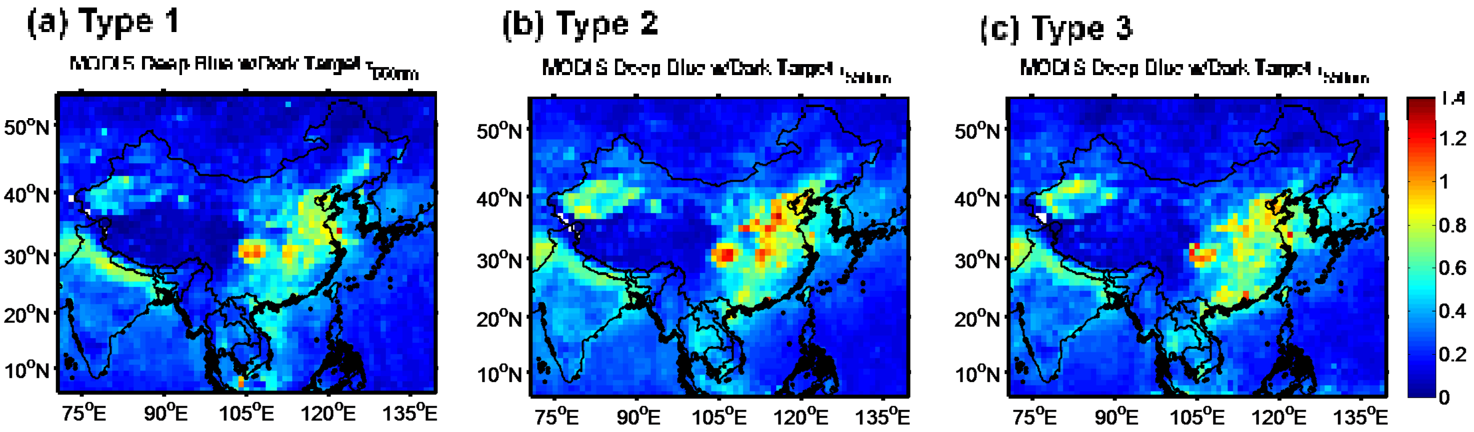

Figure 5. Composite MODIS-Aqua aerosol Deep-Blue and Dark-Target retrievals of τ_{550nm} averaged for (a) Type 1, (b) Type 2, and (c) Type 3. The third day before the case days based on the potential pollution source regions has been applied in these plots.

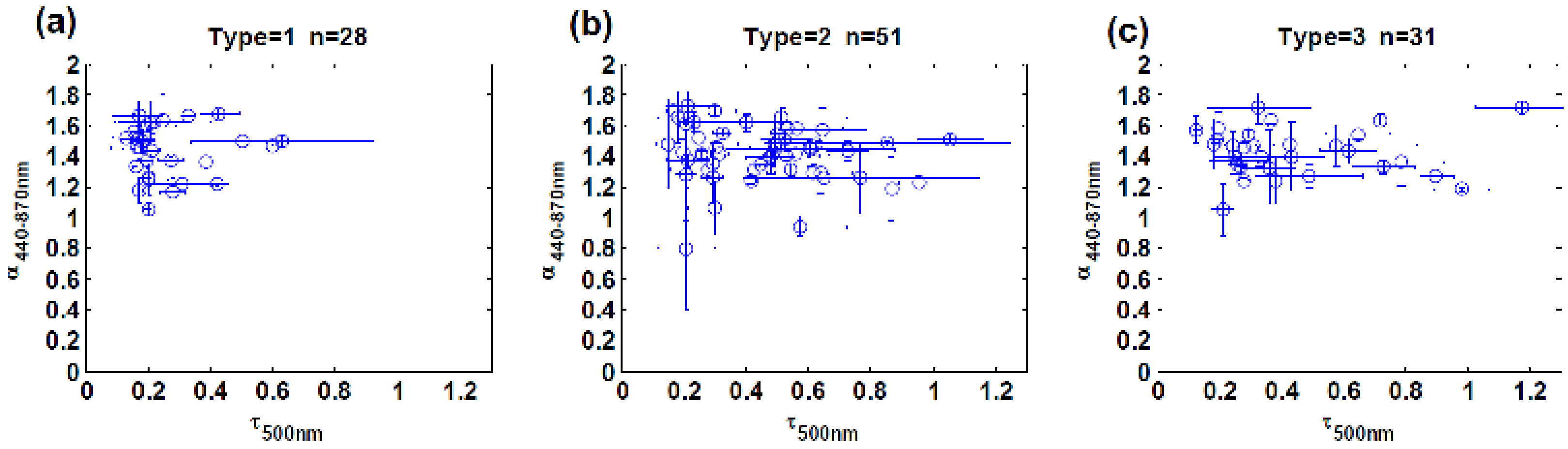

Figure 6. Scatterplots of τ_{500nm} vs. $\alpha_{440–870nm}$ at NCU for (a) Type 1, (b) Type 2 and (c) Type 3. The error bars indicate the one standard deviation.

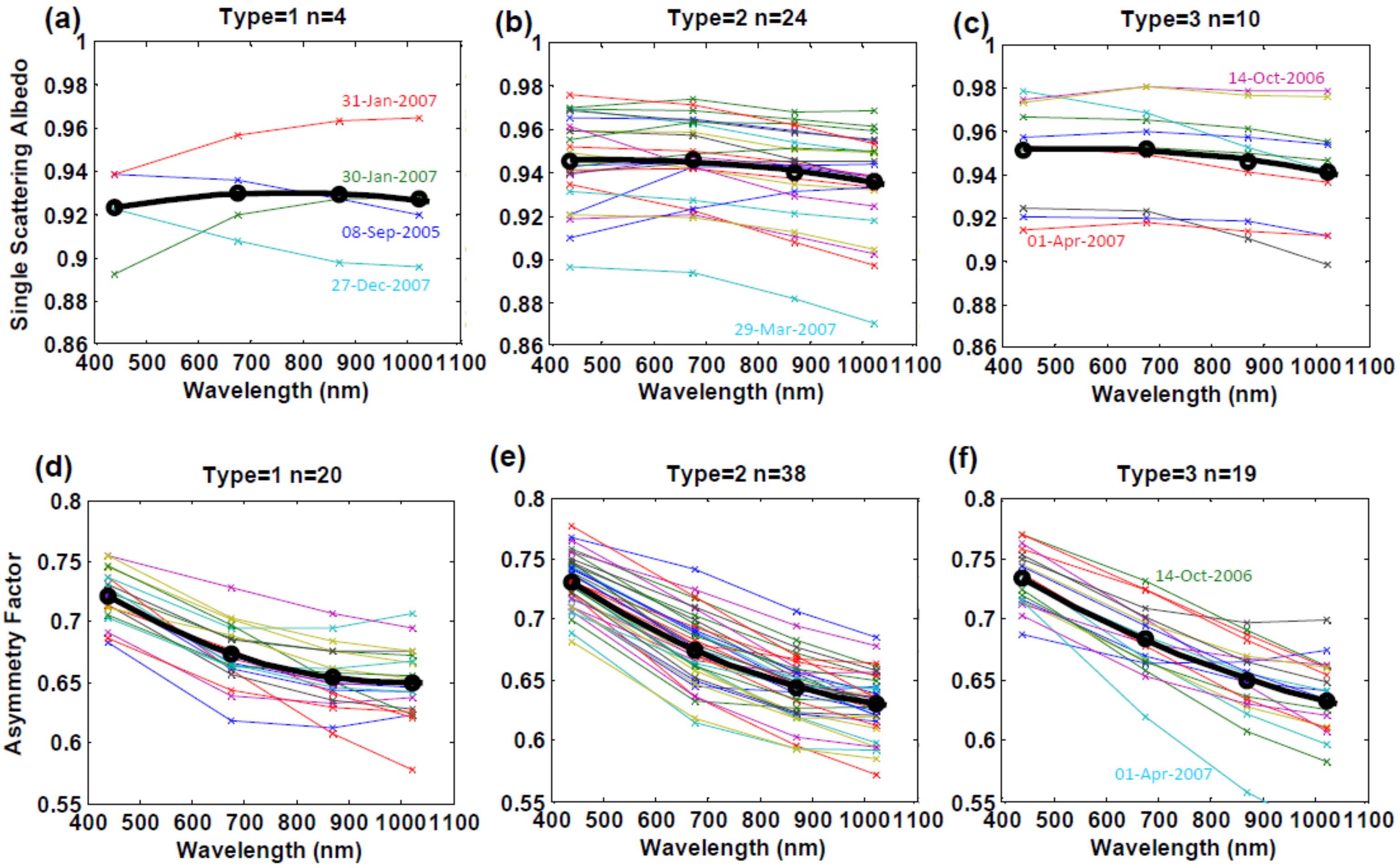

Figure 7. The AERONET inversion data (ω and g) at 440, 675, 870, 1020 nm at NCU for (a) ω of Type 1, (b) ω of Type 2, (c) ω of Type 3, (d) g of Type 1, (e) g of Type 2, and (f) g of Type 3. The daily-mean spectral ω and g are shown as cross points and thin lines. The group-mean spectral ω and g are shown as black circles and bold lines.

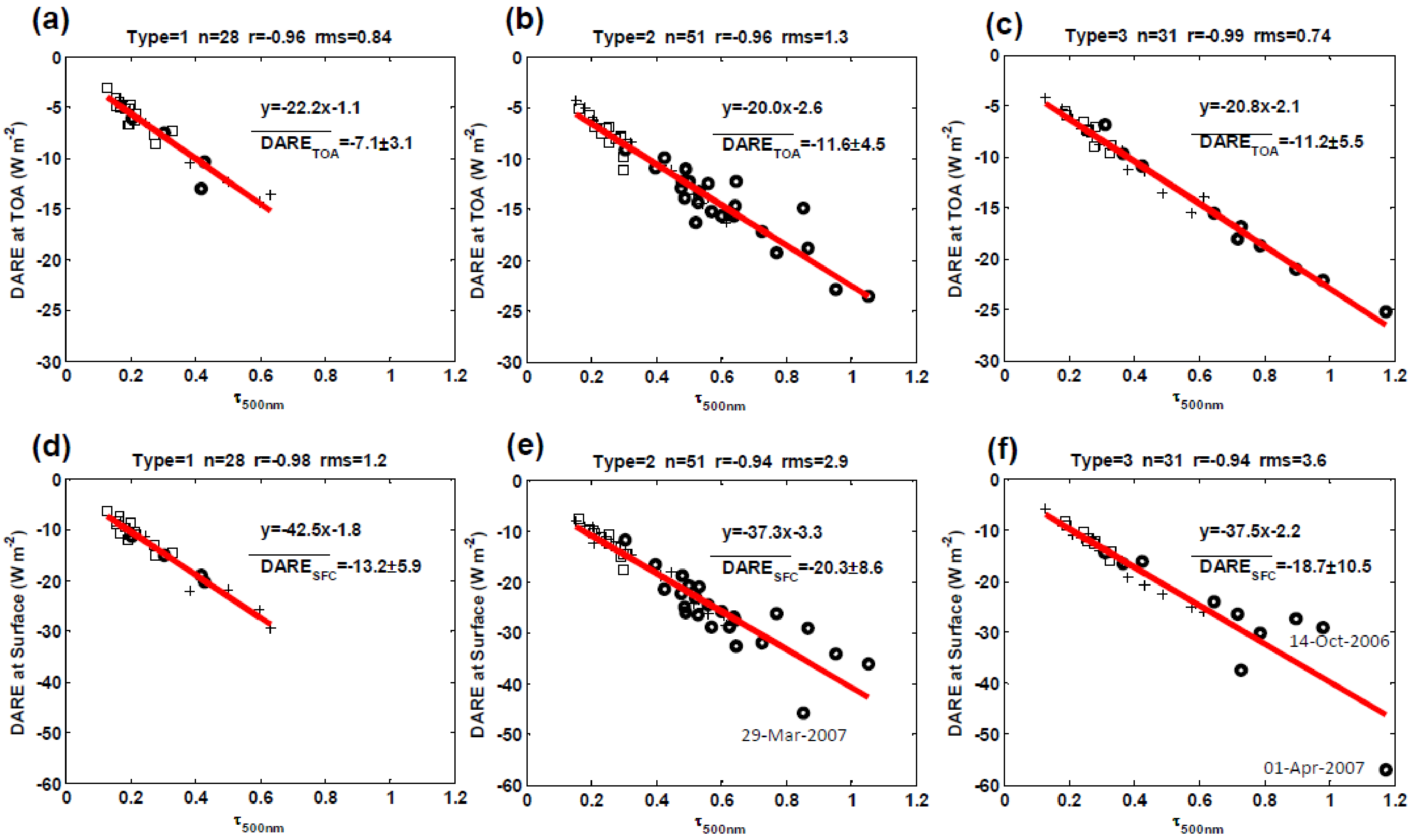

Figure 8. Scatterplots of DARE at TOA vs. τ at 500 nm for (a) Type 1, (b) Type 2, and (c) Type 3. Scatterplots of DARE at the surface vs. τ_{500nm} for (d) Type 1, (e) Type 2, and (f) Type 3. Circles represent radiative calculations based on daily-mean spectral *ω* and *g*, crosses represent data based on only group-mean spectral *ω* and *g*, and squares represent data based on daily-mean spectral *g* and group-mean spectral *ω*.

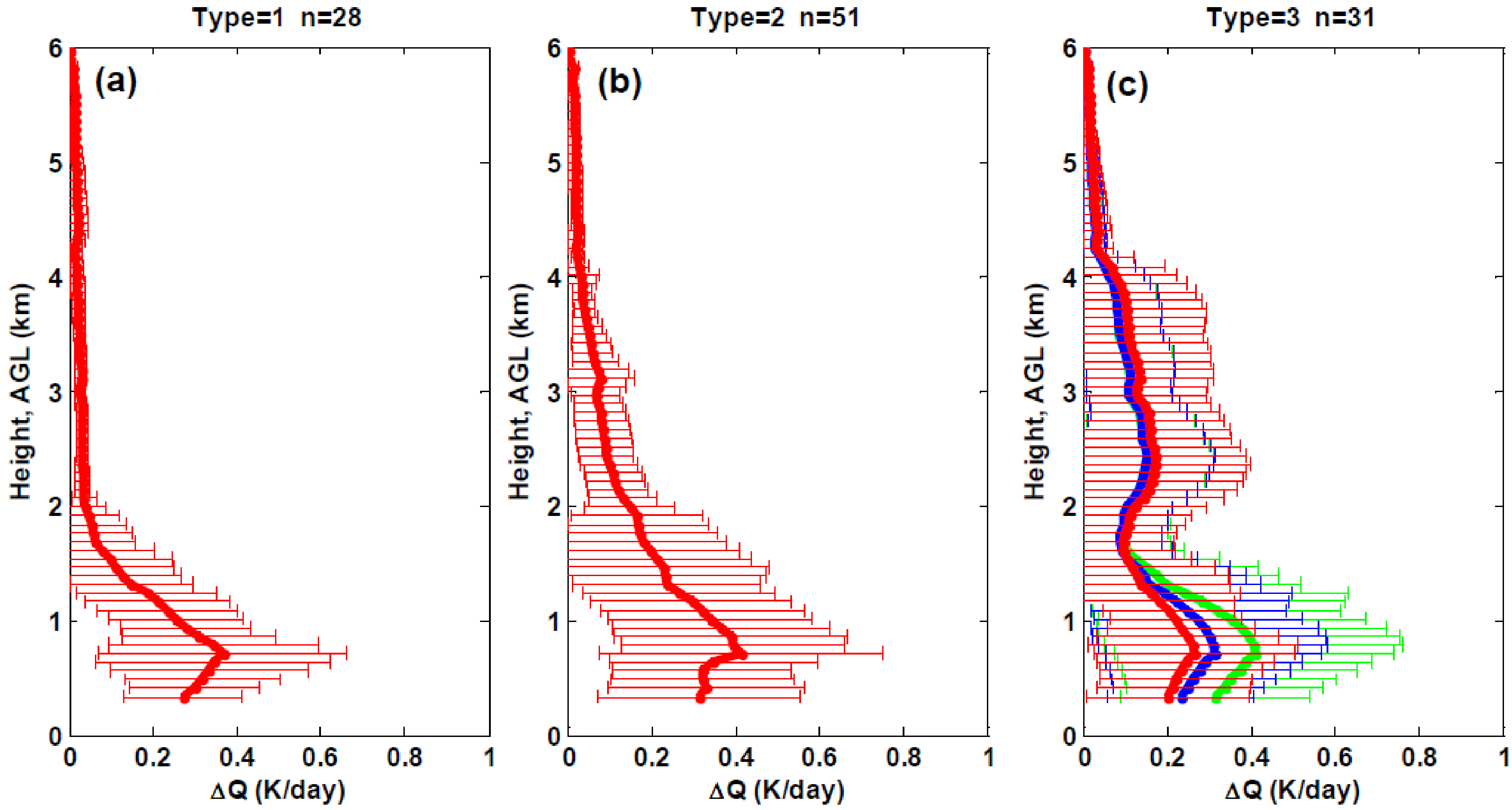

Figure 9. The vertical distribution of the mean and one standard deviation of the impact of aerosols on the atmospheric heating rate *ΔQ* (K day^{-1}) over NCU for (a) Type 1, (b) Type 2 and (c) Type 3 (red lines). The green line* and the blue line** show the improved *ΔQ* profiles for Type 3. See Table 3 for detailed descriptions of * and **.